IJMMM International Journal of Minerals, Metallurgy and Materials 矿物冶金与材料学报（英文版）

Nanosheet-stacked flake graphite for high-performance Al storage in inorganic molten $AlCl_3$–NaCl salt

Jun-xiang Wang, Ji-guo Tu, Han-dong Jiao, and Hong-min Zhu

Cite this article as:
Jun-xiang Wang, Ji-guo Tu, Han-dong Jiao, and Hong-min Zhu, Nanosheet-stacked flake graphite for high-performance Al storage in inorganic molten $AlCl_3$–NaCl salt, *Int. J. Miner. Metall. Mater.*, 27(2020), No. 12, pp. 1711-1722. https://doi.org/10.1007/s12613-020-2080-6

International Journal of Minerals, Metallurgy and Materials
Volume 27, Number 12, December 2020, Page 1711
https://doi.org/10.1007/s12613-020-2080-6

Nanosheet-stacked flake graphite for high-performance Al storage in inorganic molten $AlCl_3$–NaCl salt

Jun-xiang Wang[1)], *Ji-guo Tu*[1)], *Han-dong Jiao*[2)], *and Hong-min Zhu*[1,3)]

1) State Key Laboratory of Advanced Metallurgy, University of Science and Technology Beijing, Beijing 100083, China
2) Institute of Advanced Structure Technology, Beijing Institute of Technology, Beijing 100081, China
3) Department of Metallurgy, Graduate School of Engineering, Tohoku University, Sendai, Miyagi 9808579, Japan
(Received: 23 March 2020; revised: 17 April 2020; accepted: 22 April 2020)

Abstract: Aluminum storage systems with graphite cathode have been greatly promoting the development of state-of-the-art rechargeable aluminum batteries over the last five years; this is due to the ultra-stable cycling, high capacity, and good safety of the systems. This study discussed the change of electrochemical behaviors caused by the structural difference between flake graphite and expandable graphite, the effects of temperature on the electrochemical performance of graphite in low-cost $AlCl_3$–NaCl inorganic molten salt, and the reaction mechanisms of aluminum complex ions in both graphite materials by scanning electron microscopy, X-ray diffraction, Raman spectroscopy, cyclic voltammetry, and galvanostatic charge−discharge measurements. It was found that flake graphite stacked with noticeably small and thin graphene nanosheets exhibited high capacity and fairly good rate capability. The battery could achieve a high capacity of ~219 $mA{\cdot}h{\cdot}g^{-1}$ over 1200 cycles at a high current density of 5 $A{\cdot}g^{-1}$, with Coulombic efficiency of 94.1%. Moreover, the reaction mechanisms are clarified: For the flake graphite with small and thin graphene nanosheets and high mesopore structures, the reaction mechanism consisted of not only the intercalation of $AlCl_4^-$ anions between graphene layers but also the adsorption of $AlCl_4^-$ anions within mesopores; however, for the well-stacked and highly parallel layered large-size expandable graphite, the reaction mechanism mainly involved the intercalation of $AlCl_4^-$ anions.

Keywords: flake graphite; expandable graphite; molten salts; aluminum storage; intercalation

1. Introduction

Besides Li-ion batteries, secondary batteries based on other metal-ions have been widely proposed, including Na^+, K^+, Mg^{2+}, Ca^{2+}, and Al^{3+} [1−8], and these batteries have various reaction principles. Among these, aluminum-ion batteries (AIBs) have received attention because Al has three-electron redox properties and a high theoretical volumetric capacity of 8040 $mA{\cdot}h{\cdot}cm^{-3}$ and gravimetric capacity of 2980 $mA{\cdot}h{\cdot}g^{-1}$. The abundance, low cost, and low flammability of Al also suggest that rechargeable Al batteries could in principle be cost-effective and highly safe [9−13]. However, since the AIBs were first conceptualized in the early 1970s [14], there has hardly been any great breakthrough in the rechargeable Al batteries over the past 40 years. This is likely due to some problems such as a low cell discharge voltage (less than 1.0 V), cathode material disintegration, rapid capacity decay, and low specific capacity [15−19]. In 2015, Jiao's group [20] and Dai's group [21] made a major breakthrough: they proposed rechargeable Al batteries with graphite as cathode, and this has greatly promoted the development of aluminum storage systems.

Considerable experiments on graphitic materials with ultra-stable cycling and high capacity have been carried out in the last five years [22−27]. In our previous reports, we mentioned that the higher the graphitization degree of graphite nanoflakes, the higher the discharge voltage plateau and the larger the charge/discharge capacity [28−30]. Lin *et al.* [21] found that the highly stacked pyrolitic graphite foil exhibited a clear discharge voltage plateau near 2 V, but only presented a relatively low capacity of 60–66 $mA{\cdot}h{\cdot}g^{-1}$ at a lower current density. Chen e*t al.* [24] found that graphene film featuring highly crystallized defect-free lattice, high ionic transport channels, and continuous ion diffusion paths retained a high capacity (120 $mA{\cdot}h{\cdot}g^{-1}$) at ultra-high current density. Thus, it can be deduced that to achieve a high voltage characteristic, the high graphitization feature of graphitic materials is essential. Moreover, high ionic transport channels and a

Corresponding authors: Ji-guo Tu E-mail: guo15@126.com; Hong-min Zhu E-mail: hzhu@material.tohoku.ac.jp

large surface area with high micropores can accommodate more ions and effectively promote the rapid migration of ions and thereby yield a reasonably high rate performance. Additionally, previous studies have proved that molten salts possessed definite advantages of high ionic conductivity, fast electrode kinetics, and low polarization [31−36], thus making molten-salt batteries feature high capacity and good cycling stability at high current density.

In this work, the change of electrochemical performance caused by the structural difference between flake graphite (FG) and expandable graphite (EG) was explored, and the capacity change resulted from the structural characteristics were also analyzed. Moreover, the reaction mechanisms of the intercalation and deintercalation of aluminum complex ions in both graphite materials were discussed.

2. Experimental

2.1. Preparation of molten-salt electrolyte

Liquid sodium chloroaluminate ($NaAlCl_4$) electrolyte was obtained by mixing $AlCl_3$ (99.0%, Aladdin, China) and NaCl (99.5%, Aladdin, China) at the eutectic point with a mole ratio of 1.63 in an Ar-filled glove box. The mixture was then heated in an oven at 130°C, resulting in transparent, yellow liquid.

2.2. Fabrication of molten-salt Al-ion batteries

First, 70wt% active material (FG or EG, XFNANO, China), 20wt% acetylene black, and 10wt% poly(vinylidene difluoride) were homogeneously mixed in an N-methyl-2-pyrrolidone solvent. Then the obtained slurry was evenly coated onto a tantalum (Ta, 20 μm thickness, 99.9%) current collector. Molybdenum foil (50 μm thickness, 99.99%) attached to a graphite electrode was applied as current collector. Graphite electrode, Al foil (100 μm thickness, 99.99%), glass fiber (GF/A) separator from Whatman, and as-melt electrolyte were assembled with a sealed Teflon electrolytic tank in an Ar-filled glove box. The assembled battery was operated at various temperatures in an oven.

2.3. Electrochemical measurements

Linear-sweep voltammetry (LSV, CHI 660E, China) measurements of the molten salt were conducted using a Pt−Al configuration at a sweep rate of 2 $mV \cdot s^{-1}$. Cyclic voltammetry (CV, CHI 660E, China) tests of the cathode materials were performed using a two-electrode configuration in a voltage range of 0.4 to 2.15 V vs. Al^{3+}/Al. The charge−discharge processes were implemented at various current densities using a Neware BTS-53 tester.

2.4. Material characterization

The crystal structures of the graphite samples were analyzed using X-ray diffraction (XRD, Rigaku, D/max-RB, Japan), Raman spectroscopy (HORIBA, LabRAM HR Evolution, Japan), and X-ray photoelectron spectroscopy (XPS, Kratos AXIS Ultra DLD, UK). The morphologies of the electrode materials before and after cycling were characterized by field-emission scanning electron microscopy (JEOL, JSM-6701F, Japan) coupled with energy-dispersive X-ray spectroscopy (EDX). Nitrogen adsorption−desorption measurements of both graphite samples were performed at liquid nitrogen temperature (77.3 K) on an automatic porosity analyzer (Quantachrome, Autosorb IQ MP, America).

3. Results and discussion

The FG was stacked with graphene nanosheets, as shown in Fig. 1(a), displaying short diffusion distance in the graphitic layers. As displayed in Fig. 1(b), the EG retained the long-range-ordered layered structure of graphite, presenting longer diffusion distance. Moreover, the FG was fine and powdery (Fig. 1(c)), whereas the EG was a remarkably large-size flake (Fig. 1(f)). The SEM images in Figs. 1(d) and 1(e) and Figs. 2(a) and 2(b) indicate that the FG was made up of nanosheet-stacked multi-layer graphene. By comparison, the EG consisted of a compact bulk with the large size of ~0.5 mm (Figs. 1(g) and 1(h) and Figs. 2(c) and 2(d). The top views in Figs. 1(d) and 1(g) show that the FG was loose, but the EG was dense. The morphology results imply that compared with the EG, the FG stacked with smaller and thinner nanosheets can possess remarkably favorable characteristics in more ionic transport channels and smaller ion diffusion paths.

Fig. 3(a) presents the XRD patterns of FG and EG samples. Both the FG and EG showed typical graphitic features, with almost consistent (002) characteristic peaks of 26.54° and 26.28°, respectively. Based on Bragg's equation, the spacing between graphene sheets is 0.335 and 0.339 nm respectively. However, compared with the EG, the FG presented a sharper (002) peak, indicating a lower full width at half-maximum and thus higher crystallinity. The Raman spectra of the FG and EG samples were characterized to distinguish the graphitization features, as shown in Fig. 3(b). Both the FG and EG showed typical features of graphite, consisting of the inconspicuous D peak centered at 1350 cm^{-1}, due to the A_{1g} mode breathing vibrations of sp^3-bonded carbon. The prominent G peak located at 1581 cm^{-1} is attributed to the E_{2g} in-plane vibrational mode of sp^2 carbons in the two-dimensional hexagonal lattice [37−39]. Moreover, the D peak to G peak intensity ratios (I_D/I_G) for the FG and EG were respectively 0.14 and 0.19, indicating a more ordered graphitic structure of the FG [28,40]. The pronounced and broad 2D peak is situated around 2718 cm^{-1}, indicating that both graphite samples presented more graphitic crystallites and fewer defects [38]. The appearance of the peak at 1605 cm^{-1}

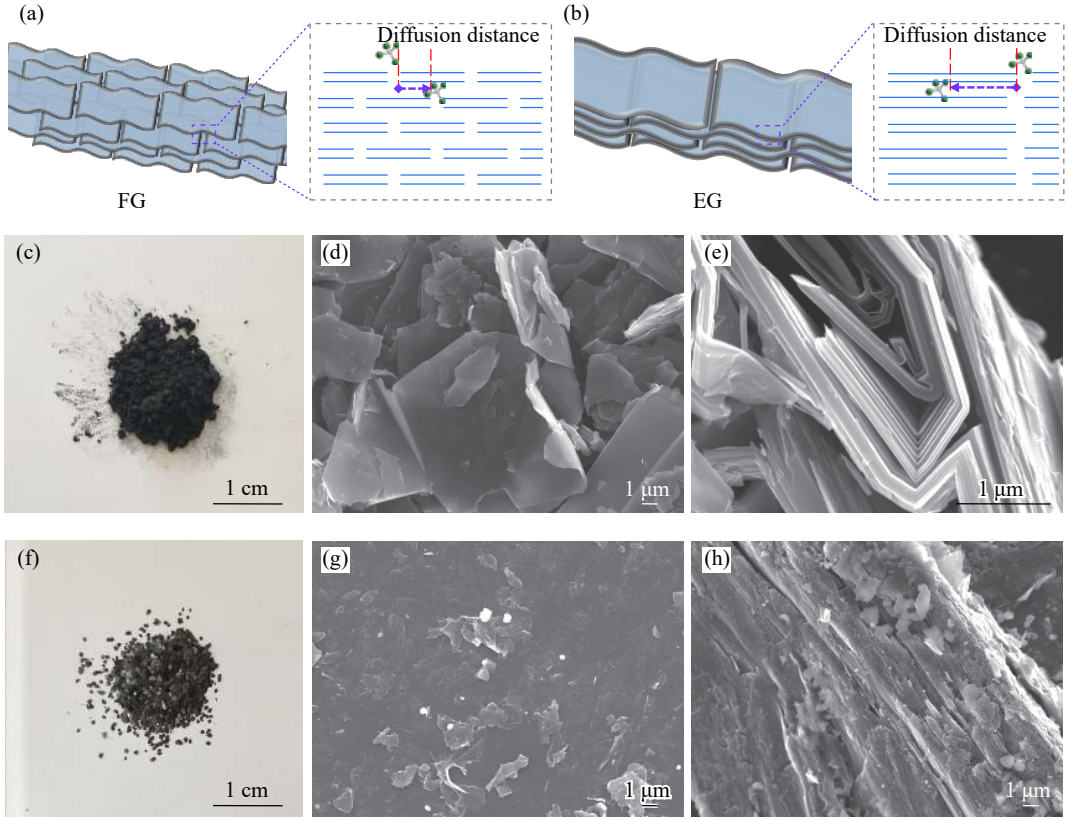

Fig. 1. Scheme of (a) FG and (b) EG structure; photographs of (c) FG and (f) EG; top-view SEM images of (d) FG and (g) EG; cross-sectional SEM images of (e) FG and (h) EG.

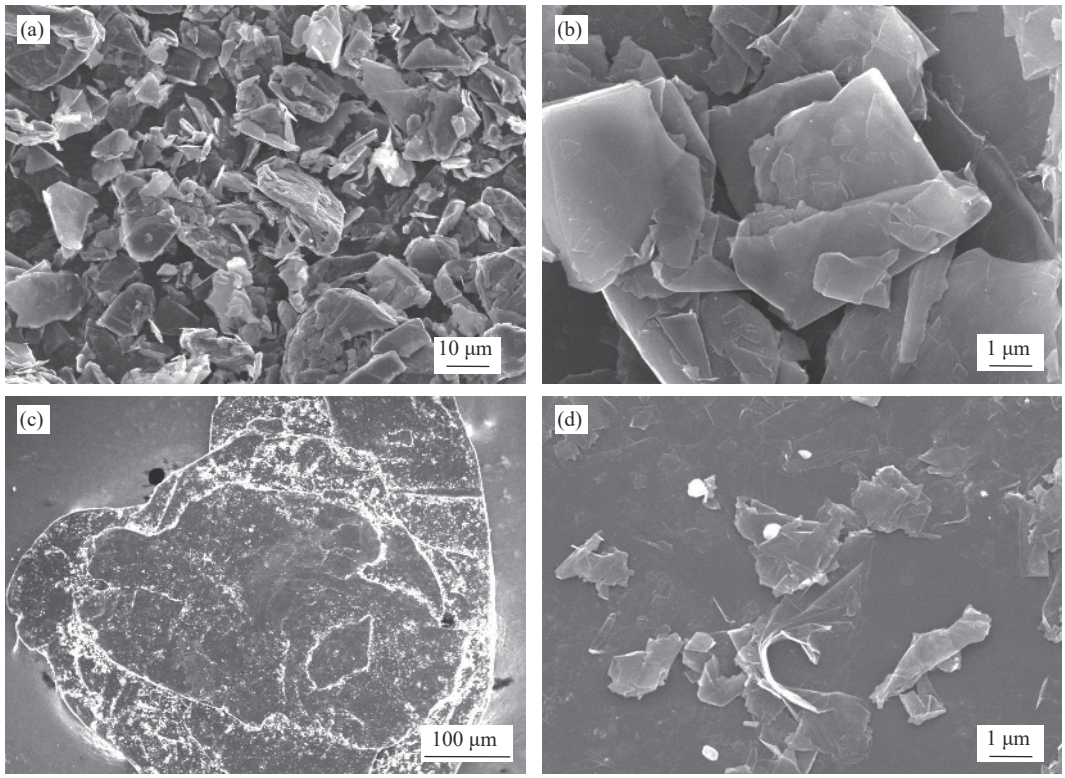

Fig. 2. Top-view SEM images of (a, b) FG and (c, d) EG at different magnifications.

can be related to a disorder or defect, as with the D peak [38,41−42]. According to the C 1s XPS spectra (Fig. 3(c)), compared with the XPS C 1s spectrum of the EG, the FG presented non-C−O and weaker sp^3 carbon characteristics, implying that it exhibited more sp^2 graphitic carbon features (284.8 eV). An oxygen-containing group existed in the EG, and the broader nature of the XPS C 1s spectrum in the EG agrees with the above-discussed XRD and Raman results.

A large specific surface area (SSA) can expose more active sties, which is beneficial for energy storage. Both samples were analyzed by N_2 adsorption−desorption measurements, and the results are shown in Fig. 3(d). Both samples displayed the same type IV feature with an associated H3-type hysteresis loop. Especially, a pronounced accretion of nitrogen adsorption for the FG sample can be observed at the high relative pressure close to 1.0, suggesting the formation of mesopore and macropore structures. Moreover, the FG (27.9 $m^2 \cdot g^{-1}$) exhibited a larger SSA than that of the EG (3.2 $m^2 \cdot g^{-1}$). According to the pore size distribution curves, the FG mesopores were mainly centered at about 4.8 nm, with a moderate number at 30.0 nm, and most of the EG pores had a size of 4.9 nm (Table 1). The abundant mesopores can enhance the kinetics of the electrolyte across graphene layers for promoting adsorption performance.

The electrochemical properties of the molten $AlCl_3$–NaCl liquid electrolyte were investigated by LSV. Fig. 4(a) shows that with the decrease in temperature, the polarization current tended to reduce, while the polarization potential tended to rise, implying that the higher temperature is not conducive to the stability of the molten salt. The CV curves of the FG electrode at temperatures ranging from 110 to 130°C were measured at 2 $mV \cdot s^{-1}$, and the results are shown in Fig. 4(b); with the reduction in temperature, the oxidation/reduction potentials were basically unchanged, while the peak current was much decreased. Fig. 4(c) shows the representative charge−discharge curves at 1 $A \cdot g^{-1}$ under temperatures between 130 and 110°C, all displaying similar charge−discharge behaviors. Moreover, the figure shows the relatively

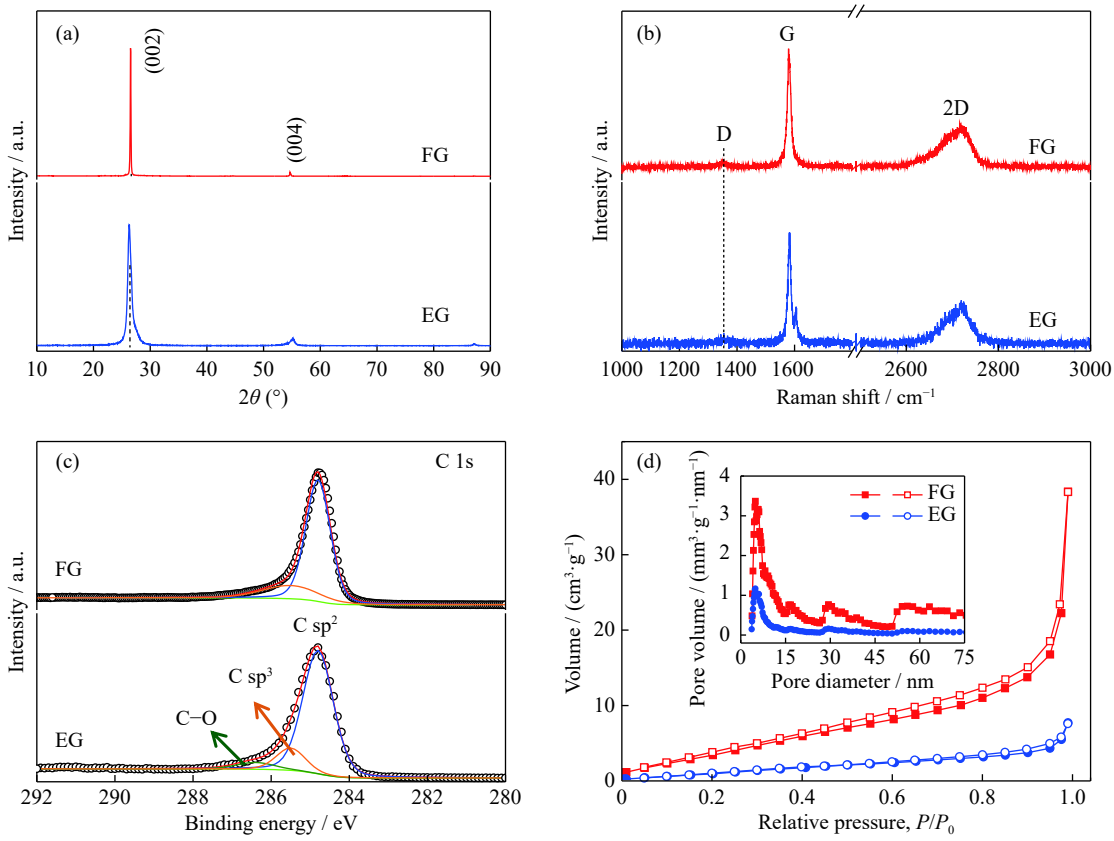

Fig. 3. (a) XRD patterns, (b) Raman spectra, and (c) XPS C 1s spectra, (d) nitrogen adsorption−desorption isotherms of the pristine FG and EG samples. Inset of (d): pore size distribution curves of the pristine FG and EG samples.

Table 1. Physical properties of FG and EG

Sample	Specific surface area / ($m^2 \cdot g^{-1}$)	Pore volume / ($mm^3 \cdot g^{-1}$)	Pore diameter / nm	Average pore diameter / nm
FG	27.9	0.065	4.8	15.1
EG	3.2	0.011	4.9	9.9

higher discharge voltage plateau and discharge capacity at a higher temperature. Fig. 4(d) illustrates the cycling stability at 200 mA·g^{-1} under temperatures ranging from 130 and 110°C. The capacity tended to increase upon cycling, indicating an activation process. When the temperature was reduced to 115°C, the capacity significantly reduced. A higher temperature is usually favorable for ion diffusion and capacity enhancement. However, a too-high temperature will cause the molten-salt electrolyte to decompose, accompanied by Cl_2 gas evolution, leading to increasing irreversible capacity and consequently a reduction in the Coulombic efficiency and cycling stability [33]. Meanwhile, the FG could afford a discharge capacity of ~180 mA·h·g^{-1} at 120°C, presenting a high capacity, Coulombic efficiency, and cycling stability. Therefore, the subsequent measurements were operated at 120°C.

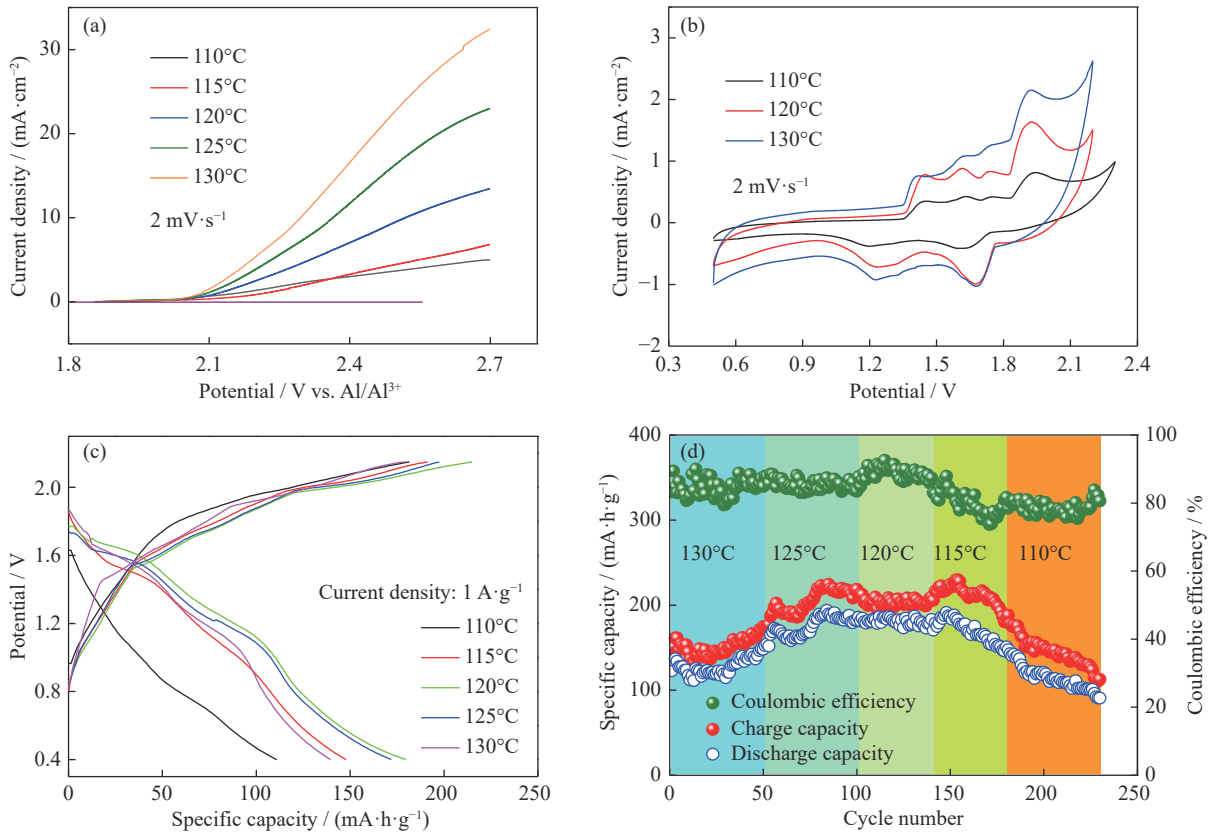

Fig. 4. (a) Polarization curves of the as-melt electrolyte determined by LSV with a scan rate of 2 mV·s^{-1} at different temperatures; (b) CV curves of FG with a scan rate of 2 mV·s^{-1} at different temperatures; (c) typical charge–discharge profiles of FG with a current density of 1 A·g^{-1} at different temperatures; (d) cycling performance of FG at a current density of 200 mA·g^{-1}.

CV measurements were performed to distinguish the reaction processes of the FG and EG, as displayed in Fig. 5. Both graphite electrodes presented four anodic peaks and three cathodic peaks. The anodic peak at 1.91 V and cathodic peak at 1.67 V are attributed to the intercalation and deintercalation of $AlCl_4^-$ anions. The anodic peaks at 1.44, 1.62, and 1.73 V and the broad cathodic peaks at 1.24 and 1.33 V are ascribed to the adsorption and desorption of $AlCl_4^-$ anions [32–33]. Comparing the FG and EG, the anodic peaks of the EG shift positively and the cathodic peaks shift toward the negative direction. More interestingly, the peak current of the redox reaction representing the adsorption and desorption for the FG electrode was significantly stronger than that for the EG electrode, which is related to the more mesopore structures and ionic transport channels of FG.

The capacity evolutions of the FG and EG electrodes during cycling are shown in Fig. 6. The charge–discharge curves for the initial five cycles in Figs. 6(a) and 6(b) show that both graphite electrodes exhibited similar charge–discharge behaviors, but the FG exhibited the higher initial capacity of 133.8 mA·h·g^{-1} (EG: 102.5 mA·h·g^{-1}). Two charge voltage plateaus correspond to the intercalation and deintercalation reactions, and two discharge voltage plateaus correspond to the adsorption and desorption reactions. Both electrodes presented enhanced capacity (Figs. 6(c) and 6(d), which is mainly because the graphite structure expanded with the intercalation of anions, which results in faster ion diffusion and increased adsorption capacity. The 100th discharge capacities of the FG and EG were maintained at 183.4 and 159.5 mA·h·g^{-1}, respectively, with Coulombic efficiencies of

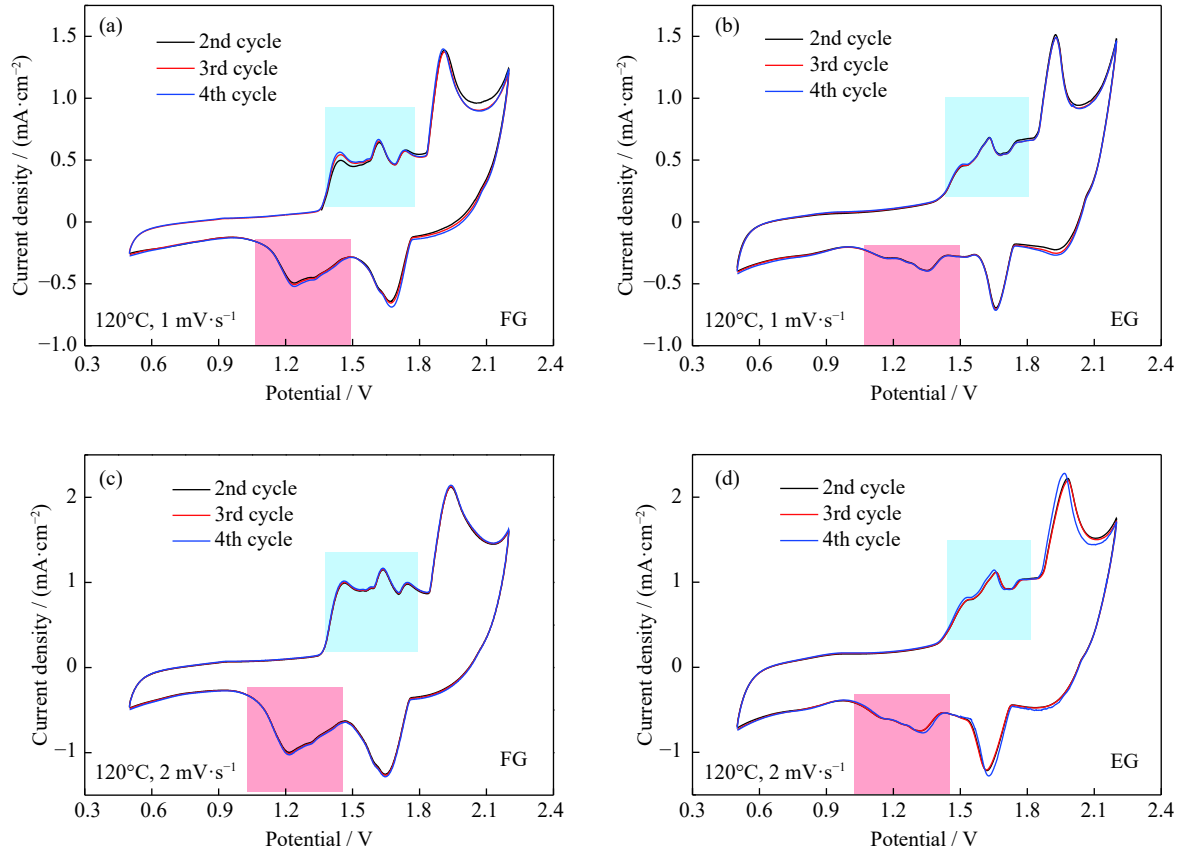

Fig. 5. CV curves of (a, c) FG and (b, d) EG with scan rates of 1 and 2 mV·s^{-1} at 120°C.

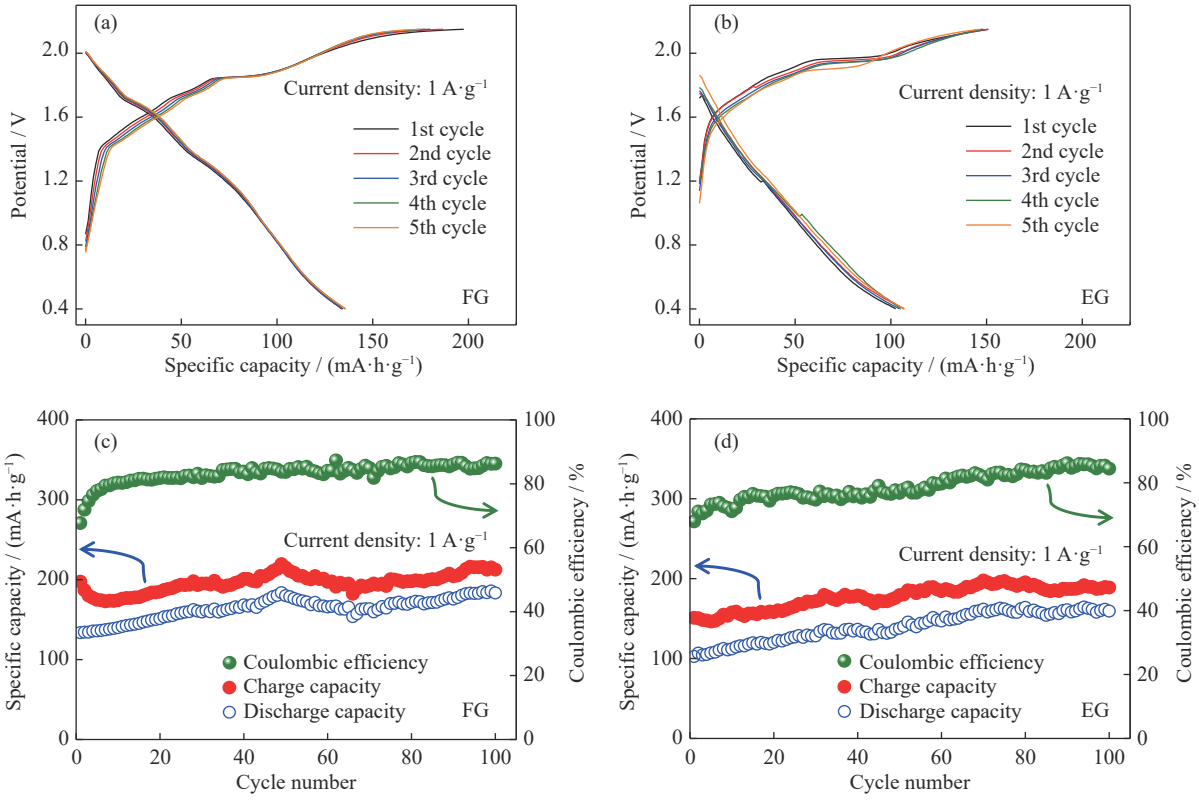

Fig. 6. First five charge–discharge curves and cycling stability of (a, c) FG and (b, d) EG at 1 A·g^{-1}.

86.3% and 84.5%, respectively. Accordingly, the following experiments were focused on FG.

Fig. 7(a) displays CV curves of FG with various sweep rates ranging from 0.5 to 10 mV·s^{-1} at 120°C. With increasing sweep rates, the anodic peaks shift in the positive direction, while the cathodic peaks shift negatively. The typical charge–discharge curves of the FG electrodes were measured at different current densities between 0.5 and 5.0 A·g^{-1} at 120°C (Fig. 7(b)). With the increase in the current density, the charge plateaus increased, the discharge plateaus decreased, and the discharge capacities decreased, presenting a similar trend with the redox peaks from the CV curves in Fig. 7(a). The capacity evolution of the FG cycles at various current densities is presented in Fig. 7(c). Even at a high current density of 5.0 A·g^{-1}, the FG could exhibit a discharge capacity of 93.8 mA·h·g^{-1}. When the current density was reverted to 1.0 A·g^{-1}, the capacity increased to ~170 mA·h·g^{-1}. The rate performance of the EG is displayed in Fig. 8. The EG exhibited a discharge capacity of ~44 mA·h·g^{-1} at 5.0 A·g^{-1}, significantly less than that of the FG. The long-term cycling stability of the FG at a high current density of 5.0 A·g^{-1} was evaluated, and the results are depicted in

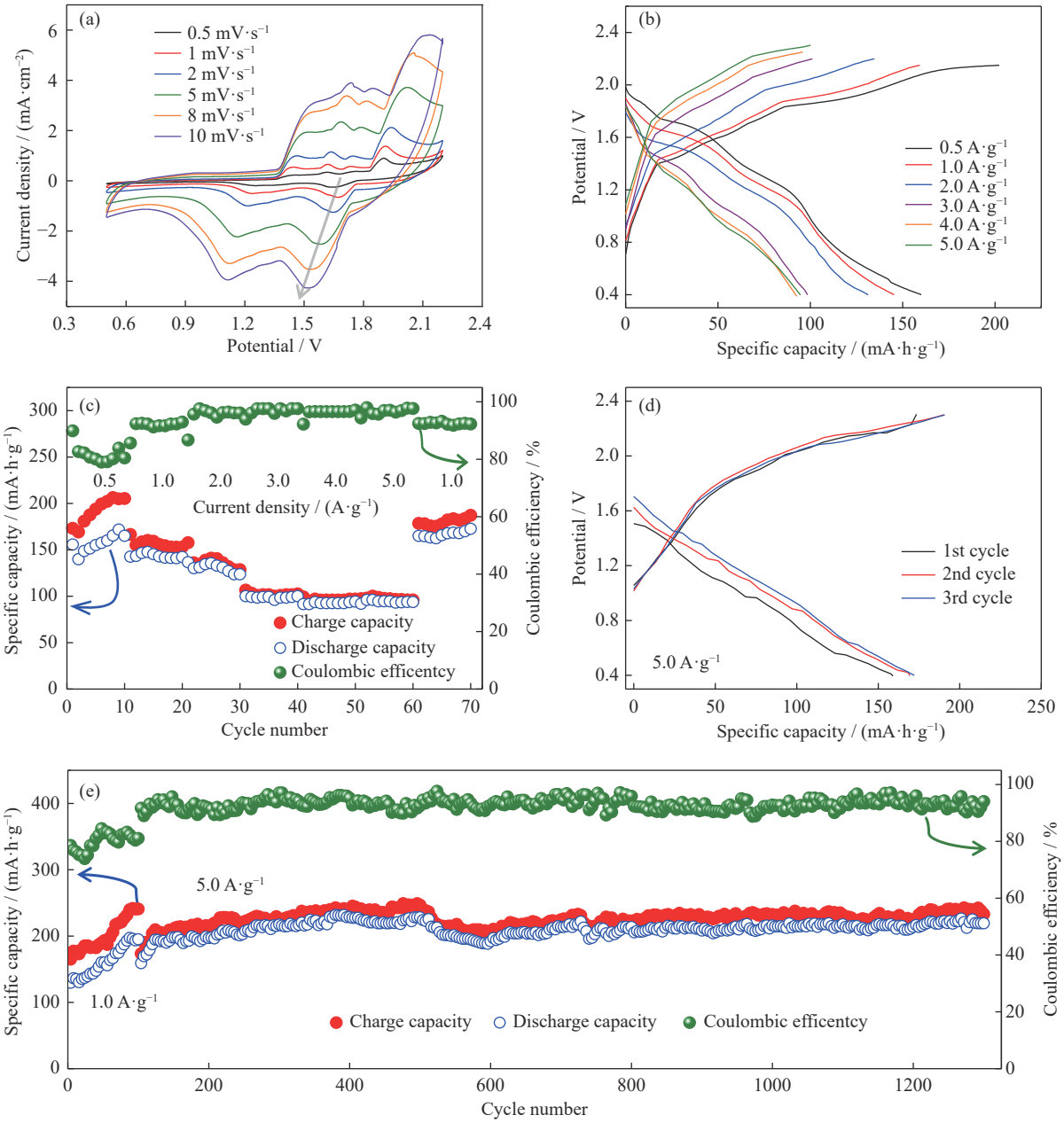

Fig. 7. (a) CV curves of FG with different sweep rates; (b) typical galvanostatic charge–discharge profiles of FG at different current densities; (c) rate capability of FG at various current densities; (d) charge–discharge profiles of FG at a high current density of 5.0 A·g^{-1}; (e) cycling performance of FG at 1.0 A·g^{-1} for 100 cycles and 5.0 A·g^{-1} for subsequent 1200 cycles.

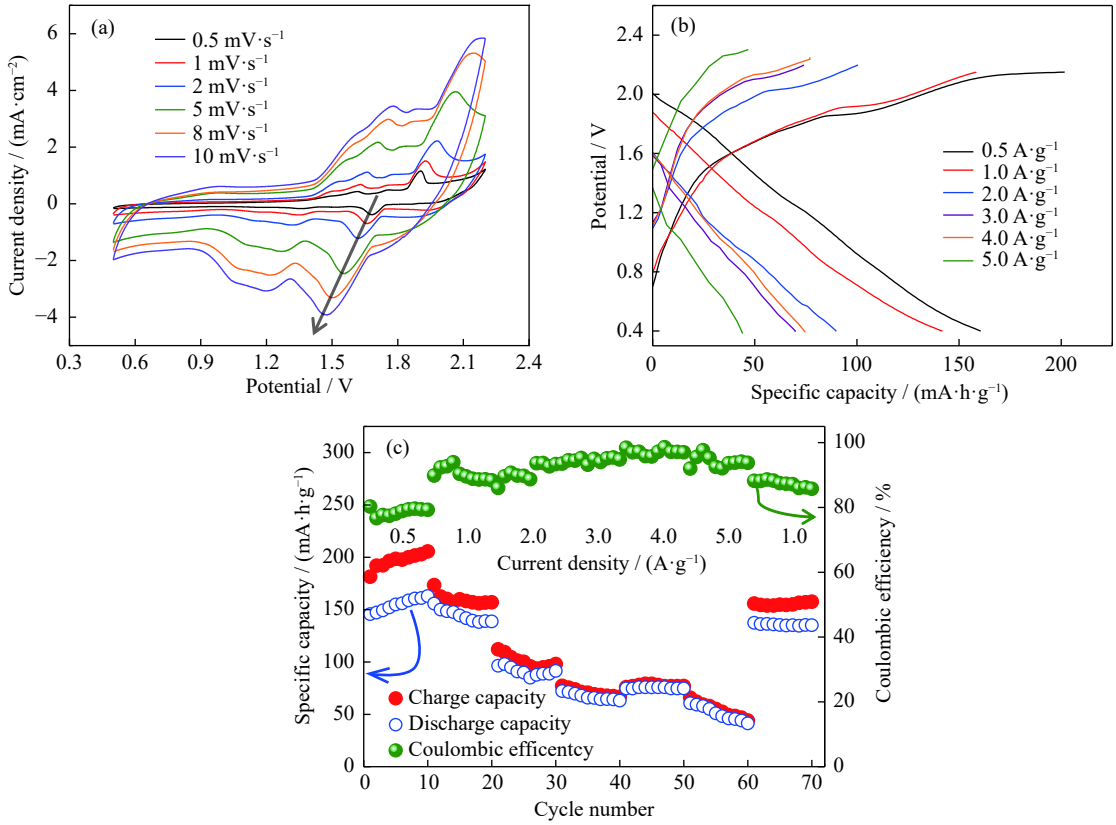

Fig. 8. (a) CV curves of EG with different sweep rates; (b) typical galvanostatic charge–discharge profiles of EG at different current densities; (c) rate capability at different current densities.

Figs. 7(d) and 7(e). After being activated for 100 cycles at a lower current density of 1.0 $A \cdot g^{-1}$, the battery exhibited an improved discharge capacity (195.2 $mA \cdot h \cdot g^{-1}$ at the 100th cycle). When cycled at 5.0 $A \cdot g^{-1}$, the battery delivered a capacity of ~160 $mA \cdot h \cdot g^{-1}$ and stabilized at ~219 $mA \cdot h \cdot g^{-1}$ for subsequent 1200 cycles with a Coulombic efficiency of 94.1%, affirming the excellent long-term cycling stability.

In addition to exhibiting an intercalation behavior, the FG with nanosheet-stacked multi-layer graphene contained a fair number of microstructural features, which can strongly increase the adsorption behavior of $AlCl_4^-$ anions within mesopores, as illustrated in Fig. 9(a). The high graphitization degree and small stacked nanosheets can enhance the cell voltage, shorten the ion diffusion paths, and improve the intercalation capacity of $AlCl_4^-$ anions; moreover, the porosity can augment the adsorption capacity (but a too-high porosity can lower the graphitization degree of the material). Therefore, maintaining synergy between the graphitization degree and porosity is essential to obtain the optimal capacity performance. Moreover, due to the well-stacked and highly parallel layered structure of the EG, the intercalation of $AlCl_4^-$ between graphene layers can be considered to be mainly responsible for the capacity (Fig. 9(b)). According to the aforementioned results, the FG stacked with smaller and thinner nanosheets presented higher mesopore structures, more ionic transport channels, smaller ion diffusion paths, and faster diffusion kinetics, facilitating the adsorption and intercalation of $AlCl_4^-$ anions, thus resulting in high capacity and good rate capability.

The FG electrodes at charged and discharged states were characterized by *ex-situ* Raman and XPS spectroscopy to further demonstrate the reaction mechanism of chloroaluminate anions into the cathode. As displayed in Fig. 10(a), when the electrode is charged, the G band is split into doublet: 1584 and 1605 cm^{-1} peaks, labeled as E_{2g2}(i) and E_{2g2}(b), respectively, verifying the intercalation of $AlCl_4^-$ anions into graphene layers. Thereinto E_{2g2}(i) can be associated with the vibrations of carbon atoms in the interior graphite layers being away from the intercalated layer planes, and E_{2g2}(b) can be attributed to the vibrations of carbon atoms in the bounding graphite layers being adjacent to intercalated layer planes [26,35,43–44]. After the electrode is fully discharged, E_{2g2}(b) peak completely diminishes, and the Raman peak returns to 1581 cm^{-1}. The XPS characterizations of Al 2p and Cl 2p peaks further demonstrate that $AlCl_4^-$ anions were intercalated into or deintercalated from graphene layers in the FG electrode (Figs. 10(b) and 10(c)).

The top-view SEM images of the original, charged, and discharged FG electrodes are displayed in Figs. 10(d)–10(f).

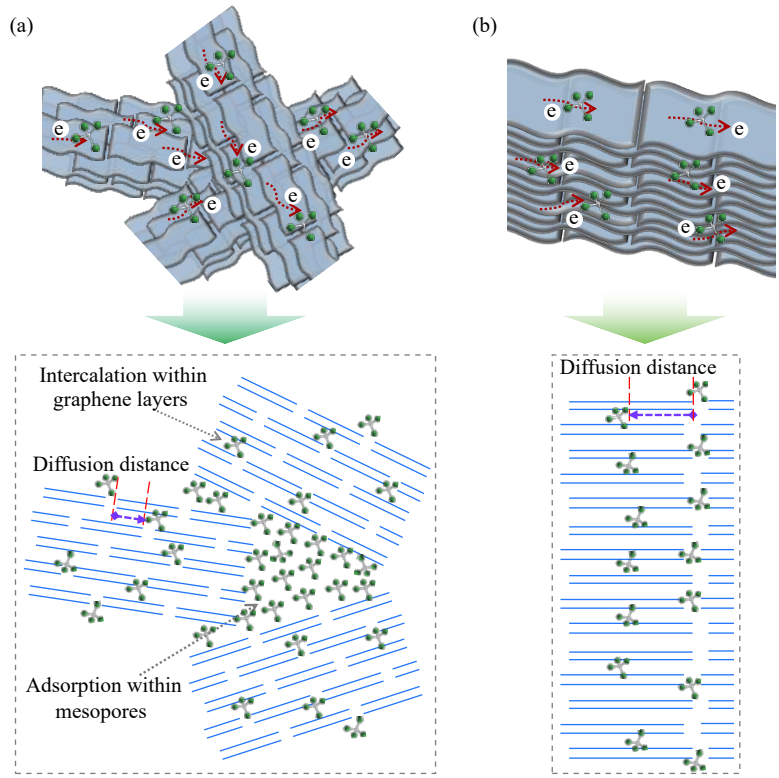

Fig. 9. Schematic diagram of $AlCl_4^-$ adsorption and intercalation of (a) FG and (b) EG during charging process.

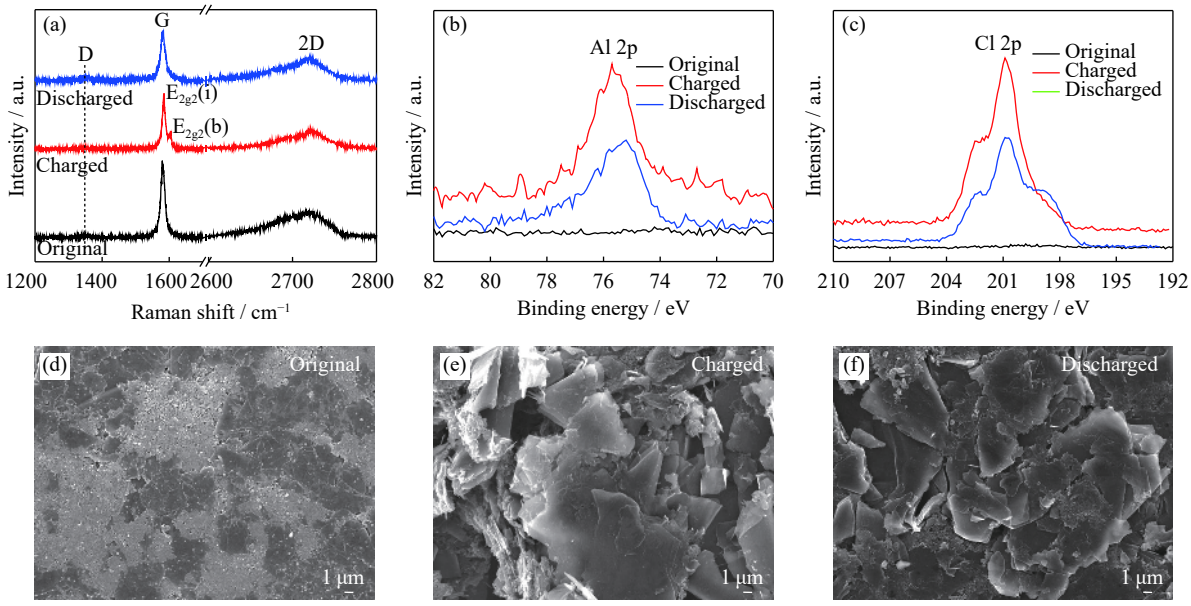

Fig. 10. (a) Raman spectra of FG electrode in the original, charged, and discharged states; XPS spectra of (b) Al 2p and (c) Cl 2p of FG electrode in the original, charged, and discharged states; (d–f) SEM images of original, charged, and discharged FG electrode.

No matter whether the electrode was fully charged or discharged, the tight surface structure of the original state was transformed into a flaky structure. Additionally, the element mapping reveals that Al and Cl elements were uniformly distributed in the charged electrodes (Fig. 11). The element analysis displays much lower Al and Cl characteristic X-ray signals in the fully discharged electrode (Fig. 12, Table 2, and Table 3). The results agree with the previously discussed XPS results, revealing the intercalation/deintercalation of $AlCl_4^-$ anions into/from graphene layers.

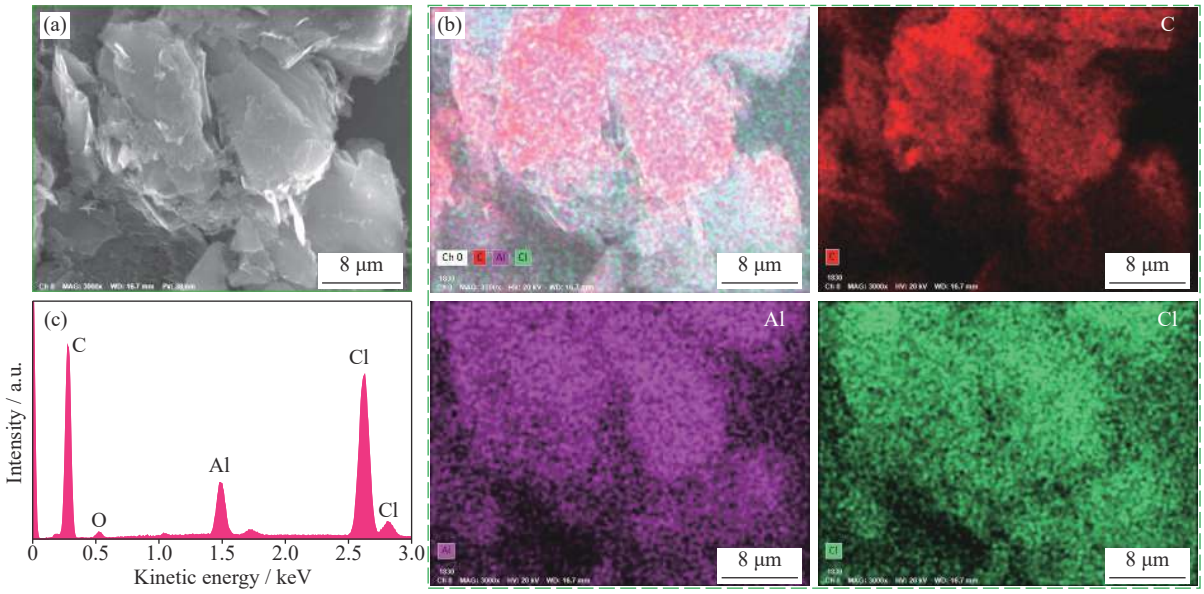

Fig. 11. (a) SEM image and (b) element mapping images of C, Al, and Cl of the charged FG electrode and (c) the EDX element analysis result.

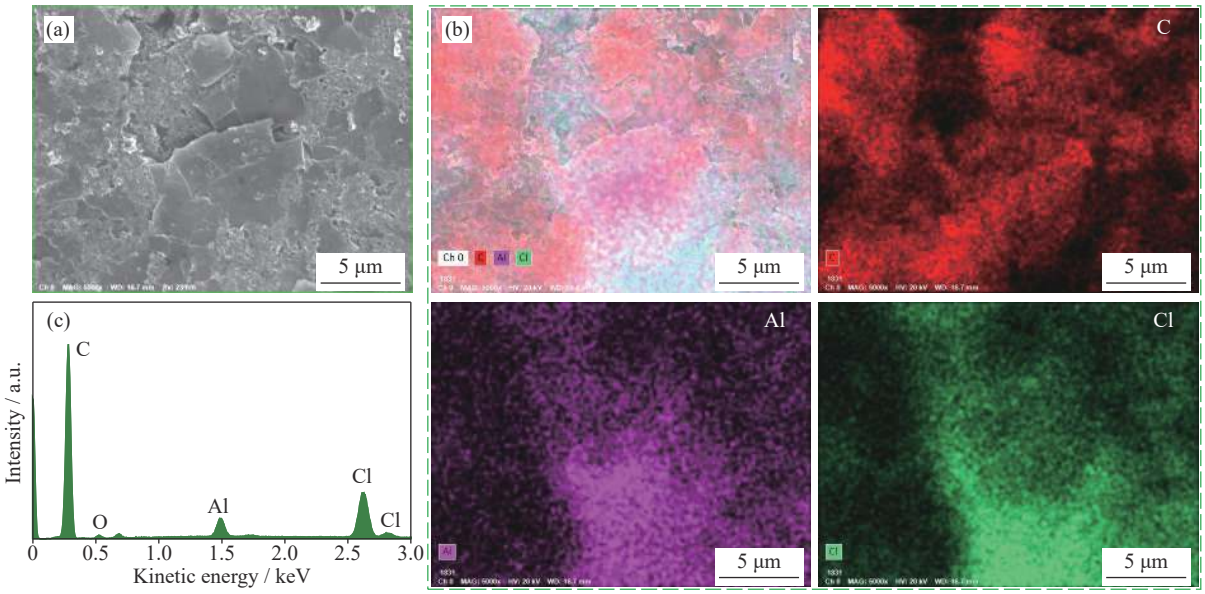

Fig. 12. (a) SEM image and (b) element mapping images of C, Al, and Cl of the discharged FG electrode and (c) the EDX element analysis result.

Table 2. EDX element analysis results of the fully charged FG.

Element	Content / wt%	Content / at%
C	81.73	91.14
O	3.60	3.01
Al	2.57	1.28
Cl	12.10	4.57
Total	100.00	100.00

Table 3. EDX elemental analysis results of the fully discharged FG.

Element	Content / wt%	Content / at%
C	89.96	94.50
O	4.02	3.16
Al	1.79	0.83
Cl	4.23	1.51
Total	100.00	100.00

4. Conclusion

The reaction mechanism of graphite in low-cost $AlCl_3$–NaCl inorganic molten salt for AIBs was confirmed. Flake graphite with small and thin graphene nanosheets and high mesopore structures enabled not only the intercalation

of $AlCl_4^-$ anions between graphene layers but also the adsorption of $AlCl_4^-$ anions within mesopores. For well-stacked and highly parallel layered large-size EG, however, the intercalation of $AlCl_4^-$ between graphene layers can be considered to be mainly responsible for the capacity. Moreover, the FG exhibited an ultrahigh capacity of ~219 $mA \cdot h \cdot g^{-1}$ over 1200 cycles at 5 $A \cdot g^{-1}$ with a Coulombic efficiency of 94.1%. Most importantly, more ionic transport channels and smaller ion diffusion paths made the FG possessed faster diffusion kinetics, presenting superior rate capability.

Acknowledgements

This work was financially supported by the National Natural Science Foundation of China (No. 51804022) and the Fundamental Research Funds for the Central Universities (No. FRF-TP-18-003C2).

References

[1] A.K. Padhi, K.S. Nanjundaswamy, and J.B. Goodenough, Phospho-olivines as positive-electrode materials for rechargeable lithium batteries, *J. Electrochem. Soc.*, 144(1997), No. 4, p. 1188.

[2] T. Stephenson, Z. Li, B. Olsen, and D. Mitlin, Lithium ion battery applications of molybdenum disulfide (MoS_2) nanocomposites, *Energy Environ. Sci.*, 7(2014), No. 1, p. 209.

[3] X. Pu, L.X. Li, H.Q. Song, C.H. Du, Z.F. Zhao, C.Y. Jiang, G.Z. Cao, W.G. Hu, and Z.L. Wang, A self-charging power unit by integration of a textile triboelectric nanogenerator and a flexible lithium-ion battery for wearable electronics, *Adv. Mater.*, 27(2015), No. 15, p. 2472.

[4] Z. Ali, T.Y. Tang, X.X. Huang, Y.Z. Wang, M. Asif, and Y.L. Hou, Cobalt selenide decorated carbon spheres for excellent cycling performance of sodium ion batteries, *Energy Storage Mater.*, 13(2018), p. 19.

[5] W.C. Zhang, J.F. Mao, S.A. Li, Z.X. Chen, and Z.P. Guo, Phosphorus-based alloy materials for advanced potassium-ion battery anode, *J. Am. Chem. Soc.*, 139(2017), No. 9, p. 3316.

[6] M.M. Huie, D.C. Bock, E.S. Takeuchi, A.C. Marschilok, and K.J. Takeuchi, Cathode materials for magnesium and magnesium-ion based batteries, *Coordin. Chem. Rev.*, 287(2015), p. 15.

[7] M. Wang, C.L. Jiang, S.Q. Zhang, X.H. Song, Y.B. Tang, and H.M. Cheng, Reversible calcium alloying enables a practical room-temperature rechargeable calcium-ion battery with a high discharge voltage, *Nature Chem.*, 10(2018), No. 6, p. 667.

[8] S. Liu, J.J. Hu, N.F. Yan, G.L. Pan, G.R. Li, and X.P. Gao, Aluminum storage behavior of anatase TiO_2 nanotube arrays in aqueous solution for aluminum ion batteries, *Energy Environ. Sci.*, 5(2012), No. 12, p. 9743.

[9] F. Ambroz, T.J. Macdonald, and T. Nann, Trends in aluminium-based intercalation batteries, *Adv. Energy Mater.*, 7(2017), No. 15, art. No. 1602093.

[10] Z.A. Zafar, S. Imtiaz, R. Razaq, S.N. Ji, T.Z. Huang, Z.L. Zhang, Y.H. Huang, and J.A. Anderson, Cathode materials for rechargeable aluminum batteries: Current status and progress, *J. Mater. Chem. A*, 5(2017), No. 12, p. 5646.

[11] Y. Zhang, S.Q. Liu, Y.J. Ji, J.M. Ma, and H.J. Yu, Emerging nonaqueous aluminum-ion batteries: Challenges, status, and perspectives, *Adv. Mater.*, 30(2018), No. 38, art. No. 1706310.

[12] H.C. Yang, H.C. Li, J. Li, Z.H. Sun, K. He, H.M. Cheng, and F. Li, The rechargeable aluminum battery: Opportunities and challenges, *Angew. Chem. Int. Ed.*, 58(2019), No. 35, p. 11978.

[13] F. Wu, H.Y. Yang, Y. Bai, and C. Wu, Paving the path toward reliable cathode materials for aluminum-ion batteries, *Adv. Mater.*, 31(2019), No. 16, art. No. 1806510.

[14] G.L. Holleck, The reduction of chlorine on carbon in $AlCl_3$–KCl–NaCl melts, *J. Electrochem. Soc.*, 119(1972), p. 1158.

[15] N. Jayaprakash, S.K. Das, and L.A. Archer, The rechargeable aluminum-ion battery, *Chem. Commun.*, 47(2011), No. 47, p. 12610.

[16] W. Wang, B. Jiang, W.Y. Xiong, H. Sun, Z.S. Lin, L.W. Hu, J.G. Tu, J.G. Hou, H.M. Zhu, and S.Q. Jiao, A new cathode material for super-valent battery based on aluminium ion intercalation and deintercalation, *Sci. Rep.*, 3(2013), p. 3383.

[17] S. Wang, Z. Yu, J. Tu, J. Wang, D. Tian, Y. Liu, and S. Jiao, A novel aluminum-ion battery: Al/$AlCl_3$–[EMIm]Cl/Ni_3S_2@graphene, *Adv. Energy Mater.*, 6(2016), No. 13, art. No. 1600137.

[18] X.D. Huang, Y. Liu, C. Liu, J. Zhang, O. Noonan, and C.Z. Yu, Rechargeable aluminumselenium batteries with high capacity, *Chem. Sci.*, 9(2018), No. 23, p. 5178.

[19] H.C. Li, H.C. Yang, Z.H. Sun, Y. Shi, H.M. Cheng, and F. Li, A highly reversible Co_3S_4 microsphere cathode material for aluminum-ion batteries, *Nano Energy*, 56(2019), p. 100.

[20] H.B. Sun, W. Wang, Z.J. Yu, Y. Yuan, S. Wang, and S.Q. Jiao, A new aluminium-ion battery with high voltage, high safety and low cost, *Chem. Commun.*, 51(2015), No. 59, p. 11892.

[21] M.C. Lin, M. Gong, B.G. Lu, Y.P. Wu, D.Y. Wang, M.Y. Guan, M. Angell, C.X. Chen, J. Yang, B.J. Hwang, and H.J. Dai, An ultrafast rechargeable aluminium-ion battery, *Nature*, 520(2015), No. 7547, p. 325.

[22] H. Jiao, C. Wang, J. Wang, J. Tu, J. Zhu, and S. Jiao, A novel rechargeable Al ion battery fabricated through molten $AlCl_3$/urea electrolytes, *Chem. Commun.*, 53(2017), p. 2331.

[23] X.Z. Yu, B. Wang, D.C. Gong, Z. Xu, and B.G. Lu, Graphene nanoribbons on highly porous 3D graphene for high-capacity and ultrastable Al-ion batteries, *Adv. Mater.*, 29(2017), No. 4, art. No. 1604118.

[24] H. Chen, H.Y. Xu, S.Y. Wang, T.Q. Huang, J.B. Xi, S.Y. Cai, F. Guo, Z. Xu, W.W. Gao, and C. Gao, Ultrafast all-climate aluminum-graphene battery with quarter-million cycle life, *Sci. Adv.*, 3(2017), No. 12, p. 7233.

[25] P. Wang, H.S. Chen, N. Li, X.Y. Zhang, S.Q. Jiao, W.L. Song, and D.N. Fang, Dense graphene papers: Toward stable and recoverable Al-ion battery cathodes with high volumetric and areal energy and power density, *Energy Storage Mater.*, 13(2018), p. 103.

[26] Z.J. Yu, S.Q. Jiao, S.J. Li, X.D. Chen, W.L. Song, T. Teng, J.G. Tu, H.S. Chen, G.H. Zhang, and D.N. Fang, Flexible stable solid-state Al-ion batteries, *Adv. Funct. Mater.*, 29(2019), No. 1, art. No. 1806799.

[27] Z.J. Yu, S.Q. Jiao, J.G. Tu, W.L. Song, H.P. Lei, H.D. Jiao, H. Chen, and D.N. Fang, Gel electrolytes with wide potential window for high-rate Al-ion batteries, *J. Mater. Chem. A*, 7(2019), No. 35, p. 20348.

[28] J.G. Tu, J.X. Wang, S.J. Li, W.L. Song, M.Y. Wang, H.M. Zhu, and S.Q. Jiao, High-efficiency transformation of amorphous carbon into graphite nanoflakes for stable aluminum-ion battery cathodes, *Nanoscale*, 11(2019), p. 12537.

[29] J.X. Wang, J.G. Tu, H.P. Lei, and H.M. Zhu, The effect of

graphitization degree of carbonaceous material on the electrochemical performance for aluminum-ion batteries, *RSC Adv.*, 9(2019), No. 67, p. 38990.

[30] R.D. Mckerracher, A. Holland, A. Cruden, and R.G.A. Wills, Comparison of carbon materials as cathodes for the aluminium-ion battery, *Carbon*, 144(2019), p. 333.

[31] B.S. Del Duca, Electrochemical behavior of the aluminum electrode in molten salt electrolytes, *J. Electrochem. Soc.*, 118(1971), No. 3, p. 405.

[32] Y. Song, S.Q. Jiao, J.G. Tu, J.X. Wang, Y.J. Liu, H.D. Jiao, X.H. Mao, Z.C. Guo, and D.J. Fray, A long-life Al ion battery based on inorganic molten salt electrolyte, *J. Mater. Chem. A*, 5(2017), No. 3, p. 1282.

[33] J.G. Tu, S.B. Wang, S.J. Li, C. Wang, D.B. Song, and S.Q. Jiao, The effects of anions behaviors on electrochemical properties of Al/graphite rechargeable aluminum-ion battery via molten $AlCl_3$-NaCl liquid electrolyte, *J. Electrochem. Soc.*, 164(2017), No. 13, p. A3292.

[34] C.F. Liao, Y.F. Jiao, X. Wang, B.Q. Cai, Q.C. Sun, and H. Tang, Electrical conductivity optimization of the Na_3AlF_6–Al_2O_3–Sm_2O_3 molten salts system for Al–Sm intermediate binary alloy production, *Int. J. Miner. Metall. Mater.*, 24(2017), No. 9, p. 1034.

[35] J. Wang, X. Zhang, W.Q. Chu, S.Q. Liu, and H.J. Yu, A sub-100°C aluminum ion battery based on a ternary inorganic molten salt, *Chem. Commun.*, 55(2019), No. 15, p. 2138.

[36] D.H. Tian, Z.C. Han, M.Y. Wang, and S.Q. Jiao, Direct electrochemical N-doping to carbon paper in Molten LiCl–KCl–Li_3N, *Int. J. Miner. Metall. Mater.*, 27(2020), No. 12, p. 1687.

[37] S. Reich and C. Thomsen, Raman spectroscopy of graphite, *Philos. Trans. R. Soc. Lond. A*, 362(2004), No. 1824, p. 2271.

[38] A.C. Ferrari, Raman spectroscopy of graphene and graphite: Disorder, electron–phonon coupling, doping and nonadiabatic effects, *Solid State Commun.*, 143(2007), No. 1-2, p. 47.

[39] K.N. Kudin, B. Ozbas, H.C. Schniepp, R.K. Prud'homme, I.A. Aksay, and R. Car, Raman spectra of graphite oxide and functionalized graphene sheets, *Nano Lett.*, 8(2008), No. 1, p. 36.

[40] Z.G. Chen, Y.X. Gu, L.Y. Hu, W. Xiao, X.H. Mao, H. Zhu, and D.H. Wang, Synthesis of nanostructured graphite via molten salt reduction of CO_2 and SO_2 at a relatively low temperature, *J. Mater. Chem. A*, 5(2017), p. 20603.

[41] L.G. Cançado, A. Jorio, and M.A. Pimenta, Measuring the absolute Raman cross section of nanographites as a function of laser energy and crystallite size, *Phys. Rev. B*, 76(2007), No. 6, art. No. 064304.

[42] A. Eckmann, A. Felten, A. Mishchenko, L. Britnell, R. Krupke, K.S. Novoselov, and C. Casiraghi, Probing the nature of defects in graphene by Raman spectroscopy, *Nano Lett.*, 12(2012), No. 8, p. 3925.

[43] M. Angell, C.J. Pan, Y.M. Rong, C.Z. Yuan, M.C. Lin, B.J. Hwang, and H.J. Dai, High efficiency aluminum-ion battery using an $AlCl_3$-urea ionic liquid analogue electrolyte, *PNAS*, 114(2017), No. 5, p. 834.

[44] X.Z. Dong, H.Y. Xu, H. Chen, L.Y. Wang, J.Q. Wang, W.Z. Fang, C. Chen, M. Salman, Z. Xu, and C. Gao, Commercial expanded graphite as high-performance cathode for low-cost aluminum-ion battery, *Carbon*, 148(2019), p. 134.